

CRAWLING THE COSMIC NETWORK: EXPLORING THE MORPHOLOGY OF STRUCTURE IN THE GALAXY DISTRIBUTION

NICHOLAS A. BOND¹, MICHAEL A. STRAUSS, RENYUE CEN

Princeton University and

Princeton University Observatory, Princeton, NJ 08544

Draft version May 30, 2019

ABSTRACT

Although coherent large-scale structures such as filaments and walls are apparent to the eye in galaxy redshift surveys, they have so far proven difficult to characterize with computer algorithms. This paper presents a procedure that uses the eigenvalues and eigenvectors of the Hessian matrix of the galaxy density field to characterize the morphology of large-scale structure. By analysing the smoothed density field and its Hessian matrix, we can determine the types of structure – walls, filaments, or clumps – that dominate the large-scale distribution of galaxies as a function of scale. We have run the algorithm on mock galaxy distributions in a Λ CDM cosmological N-body simulation and the observed galaxy distributions in the Sloan Digital Sky Survey. The morphology of structure is similar between the two catalogues, both being filament-dominated on $10-20 h^{-1}$ Mpc smoothing scales and clump-dominated on $5 h^{-1}$ Mpc scales. There is evidence for walls in both distributions, but walls are not the dominant structures on scales smaller than $\sim 25 h^{-1}$ Mpc. Analysis of the simulation suggests that, on a given comoving smoothing scale, structures evolve with time from walls to filaments to clumps, where those found on smaller smoothing scales are further in this progression at a given time.

Subject headings:

1. INTRODUCTION

Inflationary models of the early universe (Guth 1981) suggest that the large-scale distribution of matter should be well described by a gaussian random field, the statistical properties of which can be completely specified by the power spectrum. As structure evolves, however, non-linear effects become increasingly important and higher-order statistics must be computed if we wish our description to be complete. A number of studies have been performed to measure the three-point correlation function of galaxies (e.g. Peebles & Groth 1975; Gaztanaga & Frieman 1994; Nichol et al. 2007; Kulkarni et al. 2007) and its Fourier Transform (the bispectrum), as well as N -point statistics (e.g., Fry & Gaztanaga 1993; Verde, Heavens, & Matarrese 2000; Ross, Brunner, & Myers 2007). However, the filaments, walls, and clusters that appear in the non-linear regime produce very high-order correlations which are difficult to compute and interpret.

Three-dimensional maps of the galaxy distribution show walls and filaments (e.g., Thompson & Gregory 1978; de Lapparent, Geller, & Huchra 1986; Geller & Huchra 1989; Colless et al. 2001; Gott et al. 2005), as do cosmological N-Body simulations (e.g., Davis et al. 1985; Bond, Kofman, & Pogosyan 1996; Arag^on-Calvo et al. 2007; Hahn et al. 2007). At present, our methods of quantifying filamentarity (e.g., Klypin & Shandarin 1993; Shandarin & Yess 1998; Starck et al. 2004; Novikov, Colombi, & Dor^o 2006) are crude, and available methods of tracing individual filaments are even more so. Filaments produce deep potential wells on large scales, surpassed only by clumps¹. As such, they will present a signal for gravitational lensing studies

on the largest scales (Dietrich et al. 2005; Massey et al. 2007). Furthermore, filaments can act as a pathway for matter accreting onto young galaxies and galaxy clusters (e.g. Tanaka et al. 2007; Roberts et al. 2007) and can align the spins of dark matter haloes (Hahn et al. 2007).

In the classic picture put forward by Zel'dovich (1970), an ellipsoidal overdensity will collapse along its shortest axis first, forming a ‘pancake’-like structure. Some early models of structure formation, such as the ‘hot dark matter’ models, led to a ‘top-down’ scenario, in which an excess of power at large scales led to a universe filled with giant sheets, extending for tens to hundreds of megaparsecs (Zel'dovich, Einasto, & Shandarin 1982; Frenk, White, & Davis 1983). We now think that dark matter is cold and that structure formed in a bottom-up fashion, with the smaller structures forming before the larger ones. Walls may still exist, but they are not as obvious in either the galaxy catalogues or cosmological simulations as they would be in the hot dark matter models. Furthermore, it is not clear that we can apply the simple picture of ellipsoidal collapse to structures that are experiencing tidal forces from nearby structures and continual fragmentation on smaller scales.

One approach to describing bottom-up structural evolution is known as the ‘peak–patch’ theory (Bond & Myers 1996), in which clumps, the rare overdensities in a smoothed density field, form first. Filament-like features then arise along the longest principal axis of the tidal tensor, forming bridges between the clumps, followed by wall-like structures connecting the bridges. Although this description incorporates tidal interactions between neighboring structures, it focuses on only one smoothing scale at a time and is forced to resort to increasingly complex N -point statistics to describe the development of structures on scales much larger than the smoothing length.

In this paper, we are focused on measuring the dimensionality of structures in the overall distribution of matter as a function of scale. Past studies of the correlation function have

¹ nbond@physics.rutgers.edu

¹ Clumps are defined as nearly spherical overdensities that have undergone significant collapse along all three principal axes. Bound clusters are a subset of this class of structure.

shown large-scale structure to be consistent with a fractal on $\lesssim 10 h^{-1}$ Mpc scales (Martínez & Coles 1994; Pan & Coles 2000), suggesting that many of the structures apparent to the eye are nested into larger structures. Any measure of structure that ignores this fact is giving an incomplete picture of the matter distribution.

In what follows, we will describe a procedure to quantify the prominence of structures, such as filaments or walls, in the large-scale distribution of galaxies and then apply this procedure both to simulations and to observations of the large-scale distribution of galaxies from the Sloan Digital Sky Survey (SDSS; York et al. 2000). First, in § 2, we will define the local structural parameters. Walls, filaments, and clumps will each have a unique fingerprint in the resulting parameter space (λ -space) and we will present these fingerprints, along with their dependence on the properties of a given structure, in § 3. In § 4, we describe the N-body simulations and mock galaxy catalogues with which we will develop our statistics and compare the large-scale structure data. In Sections 5 and 6, we discuss the λ -space distributions of gaussian random fields and dark matter in a cosmological simulation, respectively. We will examine these statistics and compare these distributions to those of real galaxy data in § 7. Finally, in § 8, we will summarize the results and discuss their implications for our understanding of large-scale structure. Bond, Strauss, & Cen (Paper II, in preparation) will describe a method of finding individual filamentary structures.

2. METHOD

2.1. Single-scale smoothing of the density field and its Hessian

Filaments, clusters, and walls all present sharp features in the density field along at least one of their principal axes. If we wish to bring out such features, we should generate not only the density field, but also its second derivatives. The smoothed density field is defined as,

$$\tilde{\rho}(x) = \int f(x - x') \rho(x') d^3x', \quad (1)$$

where $\rho(x)$ is the density field and $f(x)$ is the smoothing kernel. The density field is initially composed of a sum of delta functions (at the positions of the galaxies or dark matter particles), which are zero-valued at infinity, so integration by parts yields the smoothed Hessian (i.e. matrix of second partial derivatives),

$$\tilde{H}_{ij}(x) = \int f(x - x') \frac{\partial^2 \rho(x')}{\partial x'_i \partial x'_j} d^3x' = - \int \frac{\partial^2 f(x - x')}{\partial x'_i \partial x'_j} \rho(x') d^3x'. \quad (2)$$

A gaussian smoothing kernel will be used throughout this paper.

The convolution is performed on a discrete grid after first performing a Fast Fourier Transform (order $N \log N$) on the kernel and data vectors. This operation implicitly assumes periodic boundary conditions, a criterion that is met by the simulation data (which is in a periodic box), but not by the survey data. For the latter case, we will only search for structures more than two smoothing lengths from the box edge.

It has been suggested by some authors (e.g. Stein 1997) that, because filaments present themselves on a multitude of scales, one should *adaptively* smooth the galaxy density field. It's true that a visual inspection of a high-resolution density

map of large-scale structure will reveal filaments on scales as small as $\sim 1 h^{-1}$ Mpc, but these filaments will often be *embedded* in larger structures, which will be difficult to identify in a single density map that deconstructs them into their smaller components (see § 8.1 for further discussion). For these reasons, we will smooth *separately* on a series of length scales when searching for filaments and walls.

2.2. The λ parameters and axis of structure

The Hessian matrix can be visualized as an ellipsoid with the major axis aligned along the direction of lowest concavity. In filamentary regions, this direction will be *along* the filament itself, so the local orientation of a filament is given by the major axis of the Hessian ellipsoid at that point. By diagonalizing the Hessian matrix, we move into the coordinate system of this ellipsoid and obtain its principal axes (the Hessian eigenvalues) and orientation (eigenvectors).

The Hessian eigenvalues at a given grid cell will be denoted λ_i and ordered such that $\lambda_1 < \lambda_2 < \lambda_3$. Along with the density and gradient vector, these provide an indication of the shape and contrast of local structure. The orientation of the structure at a given grid cell is given by A_3 , the eigenvector corresponding to λ_3 . Although real filaments will often have a non-negligible gradient along their length, we will consider only the *axis* along the filament, hereafter referred to as the ‘axis of structure’. We wish to keep our notion of a filament very simple – locally, it is a structure that is concave down along two principal axes and nearly flat along the other one. We will make no assumptions about the sign or magnitude of the first derivative along its length, but for the sake of convention, we will define A_3 such that

$$A_3 \cdot \nabla \rho > 0. \quad (3)$$

We define the dimensionless eigenvalues,

$$\lambda'_i \equiv \frac{l^2 \lambda_i}{\bar{\rho}}, \quad (4)$$

where l is the smoothing length and $\bar{\rho}$ is the mean density. Near the centres of filaments, where the density field is concave down along two axes of the filament, we expect the following relationships between the λ' -parameters:

$$\begin{aligned} \lambda'_1 &\ll 0 \\ \lambda'_2 &\sim \lambda'_3 \ll 0 \\ |\lambda'_3| &\ll |\lambda'_1|. \end{aligned} \quad (5)$$

For walls, the density field is concave down along only one axis and slowly varying along the other two,

$$\begin{aligned} \lambda'_1 &\ll 0 \\ |\lambda'_2| &\ll |\lambda'_1| \\ |\lambda'_3| &\ll |\lambda'_1|. \end{aligned} \quad (6)$$

Filaments are essentially one-dimensional objects, so a single vector can be used to represent their orientation. However, if we wish to consider walls, an additional eigenvector, A_2 , is needed. The full set of parameters to describe the geometry of structure at a given cell is given by

$$S = (A_2, A_3, \lambda'_1, \lambda'_2, \lambda'_3). \quad (7)$$

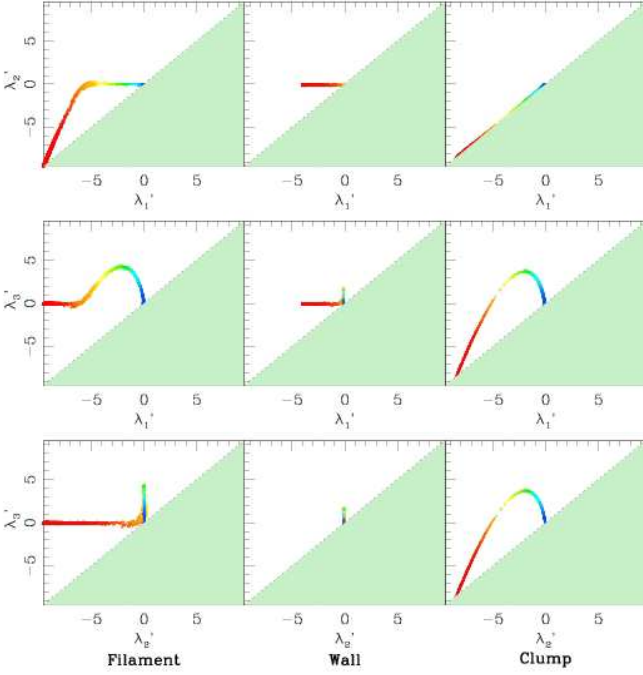


FIG. 1.— The structural ‘fingerprints’ for, from right-to-left, an isolated filament, a wall, and a cluster in an otherwise uniform background, displayed in three projections of λ -space. The points are colour-coded by local density (blue, green, yellow, orange, and red in order of increasing density) and inaccessible regions are shaded light gray, with eigenvalues defined such that $\lambda'_1 < \lambda'_2 < \lambda'_3$. All structures are smoothed on a scale much larger than their width.

3. GEOMETRY WITH λ -SPACE DISTRIBUTIONS

In Equations 5 and 6 are crude relations that we expect the λ' parameters to satisfy in the vicinity of specific large-scale structures. This can be made a bit more quantitative – filaments and walls will have simple ‘fingerprints’ in λ'_1 - λ'_2 - λ'_3 space (hereafter, λ -space) that we can look for in real data.

3.1. Three-dimensional fingerprints

In Fig. 1, we plot the λ -space projections for point distributions drawn from a two-dimensional (left), one-dimensional (centre), and three-dimensional gaussian function (right). These are models of a filament, wall, and clump, respectively, and are each placed in a $200 h^{-1}$ Mpc box. Smoothing will be done on a scale larger than the width of the structure, so the mock structures approximate a line, a plane, and a point. We confirmed that the fingerprints are coordinate-independent by rotating the mock structures to random orientations.

Fig. 1 plots the distribution of the λ parameters evaluated at the position of each galaxy, each interpolated on a $128 \times 128 \times 128$ grid. The points in this figure are colour-coded by local density (blue, green, yellow, orange, and red in order of increasing density). Note that the definition, $\lambda'_1 \leq \lambda'_2 \leq \lambda'_3$, entirely excludes four octants in λ -space, as well as portions of the remaining octants (delimited by the dashed lines in Fig. 1). In this and all subsequent multidimensional interpolations, we use a third-order polynomial routine given in Press, Flannery, & Teukolsky (1986).

In all of the λ -space distributions, there is a tight grouping of blue points near the origin made up of background objects well away from the mock structures; the Hessian matrix of a uniform density field is all zeros. The remaining points trace

the ‘fingerprint’ of the wall, filament, or clump. Each fingerprint can be understood by considering the curvature properties of a gaussian function. A gaussian function has curvature given by

$$\frac{\partial^2 f}{\partial x^2} = f(x) \left(\frac{x^2}{\sigma^4} - \frac{1}{\sigma^2} \right), \quad (8)$$

where $f(x)$ is a one-dimensional gaussian function with width, σ . At $x = 0$, the right-hand side of Equation 8 is equal to $-\rho(x)/\sigma^2$. Moving to larger values of $|x|$, the value of this function increases, reaching a maximum at $|x| = \sqrt{3}\sigma$, and then switching sign at $|x| = \sigma$. Beyond this, the curvature of a gaussian asymptotically approaches zero. The fingerprint of the wall follows naturally from this simple analysis. At all points near the wall centre (the densest regions, in red), the axis of structure will be either aligned with or orthogonal to the x coordinate axis – the density field has no y or z dependence so the curvature of the density field along those axes will always be zero. This means that $\frac{\partial^2 \rho}{\partial x^2}$ will correspond to either λ'_1 (the smallest eigenvalue) or λ'_3 (the largest eigenvalue), depending upon the sign of the curvature along the x direction (which follows Equation 8 after smoothing). Therefore, for $x < \sigma$

$$\lambda_1 = \frac{\partial^2 \rho}{\partial x^2} < 0 \quad (9)$$

$$\frac{\partial^2 \rho}{\partial y^2} = \frac{\partial^2 \rho}{\partial z^2} = \lambda_2 = \lambda_3 = 0$$

and for $x > \sigma$,

$$\frac{\partial^2 \rho}{\partial y^2} = \frac{\partial^2 \rho}{\partial z^2} = \lambda_1 = \lambda_2 = 0 \quad (10)$$

$$\lambda_3 = \frac{\partial^2 \rho}{\partial x^2} > 0.$$

This explains the origin of the half-cross shape in the centre panel of Fig. 1.

For the clump, the direction of least curvature (and, therefore, the axis of structure) will be either parallel or perpendicular to the radial vector from the clump centre. Along this radial vector, the density field will follow the curvature properties of a gaussian function, corresponding to λ'_3 in the bottom-right panel of Fig. 1. Orthogonal to this vector, the density field will always have negative curvature, meaning that the smallest two eigenvalues (λ'_1 and λ'_2 , see the top-right panel) will always be negative and, by symmetry, equal in magnitude. All three eigenvalues increase with distance from the clump centre (in red) until the curvature of the gaussian function maximizes at $r = \sqrt{3}\sigma$. Beyond this, λ'_3 drops and the fingerprint approaches the origin.

Finally, in the mock filament (left column of Fig. 1), there is no z-dependence in the density field, so one of the λ -values will always be zero and the fingerprint will be restricted to one of the λ -space coordinate planes. Near the filament centre (in red), the curvature is negative orthogonal to the filament axis. This means that the two non-zero eigenvalues are negative and the fingerprint lies in the λ'_2 - λ'_1 plane. Both of these eigenvalues will increase with distance from the filament centre, with the one corresponding to the radial eigenvector following the curvature of the one-dimensional gaussian function (Equation 8). At a cylindrical radius, $R = \sqrt{3}\sigma$, the curva-

ture changes sign and this eigenvalue becomes positive (and, therefore, becomes λ'_3), after which the fingerprint remains on the $\lambda'_3 - \lambda'_1$ plane and behaves like a projection of the clump fingerprint.

3.2. Wall and filament proportions

Neither the real data nor the cosmological simulations will have such a simple structure as the idealized models described the last section. To improve the realism of the tests, we will give the walls and filaments a finite extent, as well as place multiple structures within a single box.

The first set of tests (see Bond 2008) varied the length of the filament, ranging from six times to twice the smoothing length. As the filament size was reduced, the filament began to resemble a clump in λ -space. Filaments also have a wide range in width, as the very largest structures in the universe (e.g., the Sloan Great Wall, Gott et al. 2005) have thicknesses of $\sim 50 h^{-1}$ Mpc in redshift space, much greater than the widths of ‘typical’ filaments visible in redshift surveys. We generated sample filaments to test this width dependence, varying it between half and twice the smoothing length. We found that, even for very long filaments, the λ -space distributions show few of the characteristic ‘filament’ features unless the structure is narrower than the smoothing length. Thus, single-scale smoothing is insensitive to structures much wider than the smoothing length, suggesting that it will be useful to measure the *scale-dependence* of filamentarity with a series of measurements on different smoothing scales.

Finally, in Fig. 2, we plot the λ -space projections of three multi-filament boxes. All mock filaments have a width, $\sigma = 1 h^{-1}$ Mpc, a length of $30 h^{-1}$ Mpc, and are randomly placed and oriented in the box. The resulting composite distributions are then smoothed on a $10 h^{-1}$ Mpc scale. Since the filaments have the same properties, the sum of their fingerprints looks like that of a single filament, and in the left panel, this is all that is seen. As the number of filaments increases, however, their average separation decreases and they begin to fill more of λ -space. By $N = 50$ (right column), the points have dispersed along the $\lambda'_1 = \lambda'_2$ boundary and spread about the $\lambda'_3 = 0$ axis at high densities. The basic shape of the fingerprint remains, but the points have been dispersed by the presence of other nearby filaments.

We conducted similar tests for walls, varying their side lengths, widths, and number within a box. Points in the vicinity of a wall’s edge will have λ -parameters similar to those of a filament and parameters for points near the corners will be like those of the clump. As with the filaments, a great deal of scatter was introduced when the structures were made very wide or very numerous.

Although the morphology of the λ -space distributions can vary with a structure’s width, length, or overdensity, there are discriminating features for each type of structure. Filaments can most easily be distinguished from clumps by a concentration around the $\lambda'_3 = 0$ axis in the $\lambda'_3 - \lambda'_1$ projection, while walls can be distinguished from filaments by a concentration on the $\lambda'_2 = 0$ axis in the $\lambda'_2 - \lambda'_1$ projection. In § 7, these facts will be used to probe structure in cosmological simulations and SDSS galaxy data.

4. THE SIMULATION

Before we present the λ -space projections of the observed galaxy distribution, it is useful to explore the predictions of the standard cosmological model. A cosmological simulation

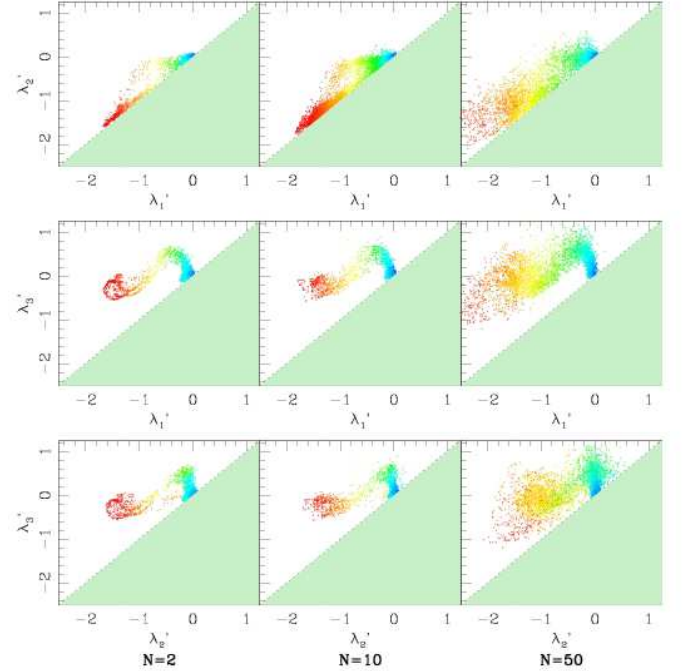


FIG. 2.— The λ -space projections of three particle distributions, each containing filaments with lengths of $60 h^{-1}$ Mpc and widths of $6 h^{-1}$ Mpc. The number of filaments in the boxes are, from left to right, 2, 10, and 50, randomly placed and oriented within a $200 h^{-1}$ Mpc box and smoothed on a $10 h^{-1}$ Mpc scale. As the filament density increases, the λ -space distributions becomes smeared relative to the fingerprint of Fig. 1. Nevertheless, a filament-dominated distribution can still be distinguished from a wall- or clump-dominated distribution by the outlying (high-density) points in the $\lambda'_3 - \lambda'_1$ projection.

allows us to develop our techniques on a data set not subject to redshift distortions, sparse sampling, and complicated window functions. Furthermore, we can simulate these effects in mock catalogues, providing a useful standard for comparison to the real SDSS data.

We use a series of cosmological CDM N -body simulations with $\Omega_m = 0.29$, $\Omega_\Lambda = 0.71$, $\sigma_8 = 0.85$, and $h = H_0/(100 \text{ km s}^{-1} \text{ Mpc}^{-1}) = 0.69$ (Spergel et al. 2007). The simulation is performed within a $200 h^{-1}$ Mpc box with 512^3 particles, each with mass, $m_p = 4.77 \times 10^9 h^{-1} M_\odot$, and is run on a 92-node Beowulf cluster located at Princeton University. The positions and velocities of dark matter particles are output at six redshifts – $z = 0, 0.3, 0.5, 1, 2$, and 3. Because of memory restrictions, we split the simulation box into a $3 \times 3 \times 3$ lattice in order to run a halo-finder and identify galaxies. Each subbox was padded with the particle data within $10 h^{-1}$ Mpc of its boundaries. The padding size is an order of magnitude larger than the largest dark matter haloes, so edge effects are negligible.

We identified dark matter haloes with the HOP algorithm (Eisenstein & Hut 1998, hereafter EH98), which searches for peaks in the density field by moving from particle to particle until it reaches one that is in a denser environment than any of its neighbors. Densities are computed with an adaptive kernel with a length scale set by the N_{dens} nearest particles, and the ‘hopping’ can occur to any of the N_{hop} nearest particles. Groups are then pruned, merged or disbanded depending on their peak and outer density thresholds (see EH98 for more details). Following EH98, we select $N_{\text{hop}} = 16$, $N_{\text{dens}} = 64$, $N_{\text{merge}} = 4$, $\delta_{\text{peak}} = 240$, $\delta_{\text{saddle}} = 200$, and $\delta_{\text{outer}} = 80$. In addition, we keep only haloes with $N \geq 8$ particles. These parameters give

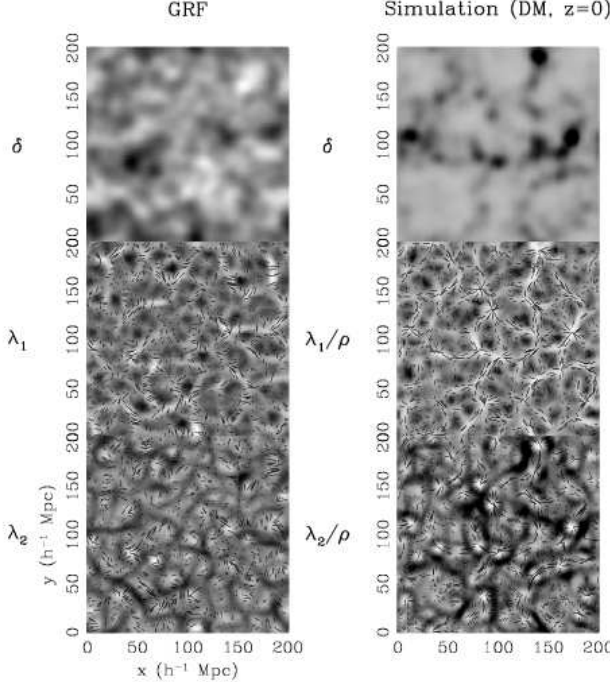


FIG. 3.— A two-dimensional gaussian random field with the $z = 0$, ΛCDM power spectrum (left column) compared with a two-dimensional slice ($10 h^{-1}$ Mpc deep) from the $z = 0$ dark matter distribution (right column) in a cosmological simulation. The top row shows the density fields smoothed on a $5 h^{-1}$ Mpc scale, while the middle and bottom rows show the corresponding λ'_1 and λ'_2 maps, respectively. Bars have been plotted over the λ -maps to indicate the direction of the axis of structure at random points on the plane. The bar's length is proportional to the magnitude of λ'_1 at that point. At all smoothing scales shown here, the axis of structure aligns with the local filamentary structure in the dark matter distributions. This alignment is absent in the gaussian random fields, despite a similar λ'_1 distribution.

halo distributions similar to those of a friends-of-friends algorithm (Huchra & Geller 1982) with a linking length of 0.2.

5. GAUSSIAN RANDOM FIELDS

In both the cosmological simulations and observed galaxy distribution, we wish to identify the morphological features that are due to non-linear collapse; that is, non-gaussianities. If we wish to reveal these features in λ -space, then we should compare the Hessian parameters in observed or simulated data to those in a gaussian random field with the same power spectrum. For the non-linear power spectrum, we use the prescription of Smith et al. (2003), with the concordance model parameters of Spergel et al. (2007).

The left column of Fig. 3 shows linear grayscale maps of a single realization of a two-dimensional gaussian random field (generated on a grid), with the non-linear power spectrum and smoothed on a $5 h^{-1}$ Mpc scale. In the top panel we plot the smoothed overdensity field, $\delta(x)$, while the smoothed λ'_1 and λ'_2 maps (not normalized to the local density) are given in the centre and bottom panel, respectively. The grayscale map of λ'_1 gives a strong impression of filamentary structure in the gaussian random field. Note, however, that the λ parameters are essentially edge-finders, and even in a gaussian random field, overdensities (whose edges are apparent in the λ'_1 map) and underdensities (λ'_2 map) will have boundaries. In a gaussian random field, the overdensities and underdensities are statistically identical, so the maps are morphologically similar.

On the righthand side of Fig. 3, we show the same grayscale maps for the dark matter distribution in a cosmological simulation (see § 4) at $z = 0$, but with the λ parameters (centre and bottom panels)

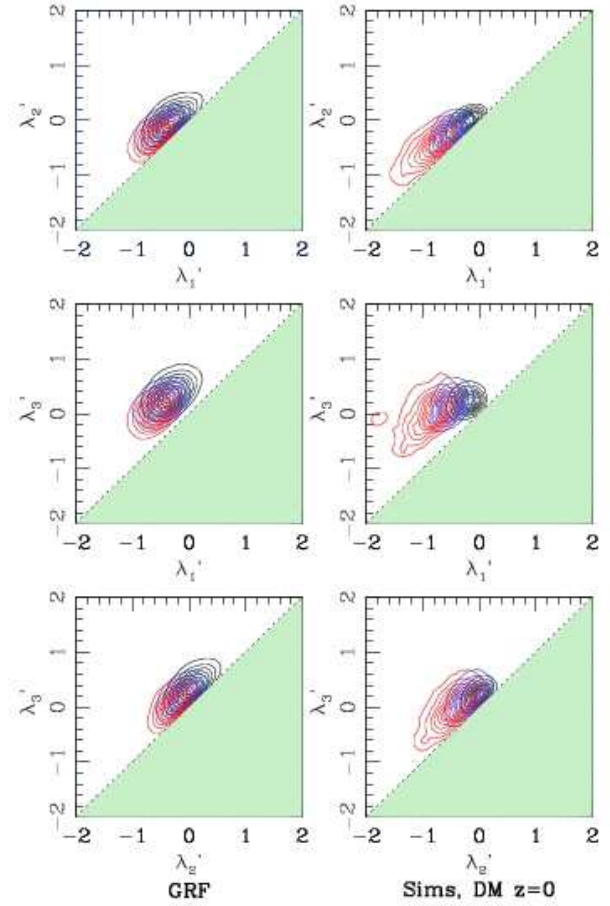


FIG. 4.— The λ -space projections for a three-dimensional gaussian random field (left) and the simulated $z = 0$ dark matter distribution (centre). Contours represent the distribution of λ at the positions of dark matter particles (not grid cells) from a sampling of the fields. In the left two columns, contours are for different density subsamples, where black contours indicate the distribution of points in underdense regions (first or second quartile), blue contours in regions of intermediate density (third quartile), and red contours in the most dense regions (upper quartile).

normalized to *local* density². Non-linear growth of structure amplifies overdense edges and the low-contrast structures tend to become washed out in the raw λ -maps. After density normalization, however, the edges show a similar morphology to those in the λ'_1 and λ'_2 maps of the gaussian random field, suggesting that the outline of the network of filaments and walls is already in place in the initial conditions (as was first suggested by, Bond et al. 1996). Also included in the bottom two rows of Fig. 3 are bars indicating the direction of the local axis of structure. In the simulations, the axis of structure is nearly perfectly aligned with the λ'_1 edges in even the weakest strands, while in the gaussian random fields, there is no obvious correlation between the axis of structure and the orientation of the edges. The direction of the axis of structure does not appear to be correlated on much more than a smoothing length in the gaussian random field, while the simulations have structures that are aligned across the entire $200 h^{-1}$ Mpc box!

6. GEOMETRY OF DARK MATTER AND MOCK GALAXY DISTRIBUTIONS

² Note that the gaussian random fields used in the left columns of Figs. 3 and 4 are *not* the seed fields for the simulations used in the right columns.

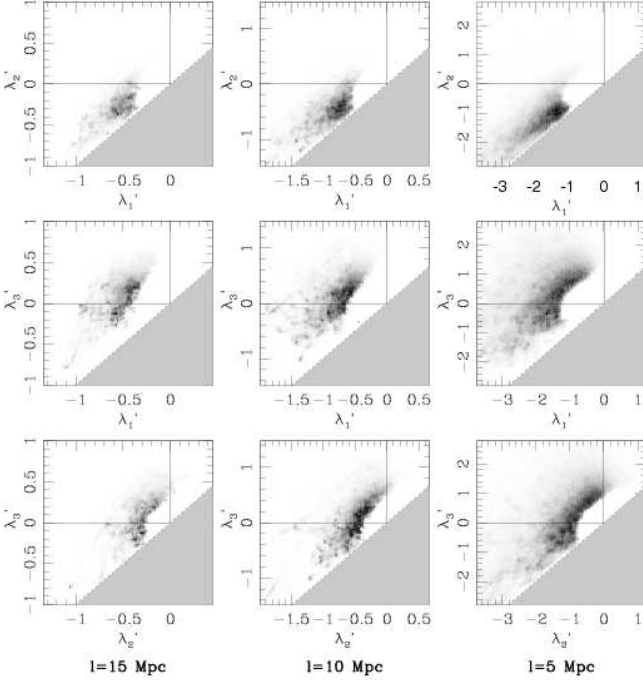


FIG. 5.— The λ -space projections for the $z = 0$ dark matter distribution, after subtraction by the λ -space distribution of a gaussian random field with the same power spectrum. Grayscale cells indicate those regions in which the dark matter distribution shows an excess over the gaussian random field and for which the local density is greater than the mean, with darker cells indicating more of an excess. Regions showing no excess or regions showing a deficit are left blank. The axes of each plot have been scaled in proportion to the amplitude of the dimensionless power spectrum at the appropriate smoothing scale.

The two-point correlation function and power spectrum already provide a direct measure of the two-point properties of the large-scale distribution of matter, so we wish to extract from λ -space only that information which cannot be obtained from two-point statistics. In the left column of Fig. 4, we show the λ -space distribution (smoothed on a $10 h^{-1}$ Mpc scale) of a three-dimensional gaussian random field. The contours illustrate λ -space distributions for points in the bottom 50 per cent of the real-space density distribution (black), between 50 and 75 per cent (blue), and the upper 25 per cent (red). The gaussian random field was sampled in a $(200 \text{ Mpc})^3$ three-dimensional grid in proportion to the local overdensity and no points were placed in grid cells having $\delta \leq -1$. Within a given panel of Fig. 4, there is little variation in the size or shape of the contours as a function of overdensity, indicating no density dependence of structural morphology. The plot is generated from only one realization of a gaussian random field, but finite volume effects are small at this smoothing scale.

In the large-scale distribution of matter, structure grows due to the gravitational effects of the total matter distribution. As such, we compute λ -space distributions at the positions of *dark matter particles* (not grid cells) in the $z = 0$, dark-matter-only simulation described in § 4; these are shown in the right column of Fig. 4. At high densities (red), the dark matter contours are extended because of the presence of overdense clumps. The low-density contours, however, are contracted relative to those of the gaussian random field. The largest underdensities in the gaussian random field have a positive curvature (and, therefore, positive λ -values) comparable to the negative curvature of the overdensities, while dark matter underdensities are voids with a very small spread in density and curvature. If non-linear growth of structure leads to the formation of filaments and/or walls in the dark matter distribution, there should be an excess in the regions of λ -space occupied by these fingerprints.

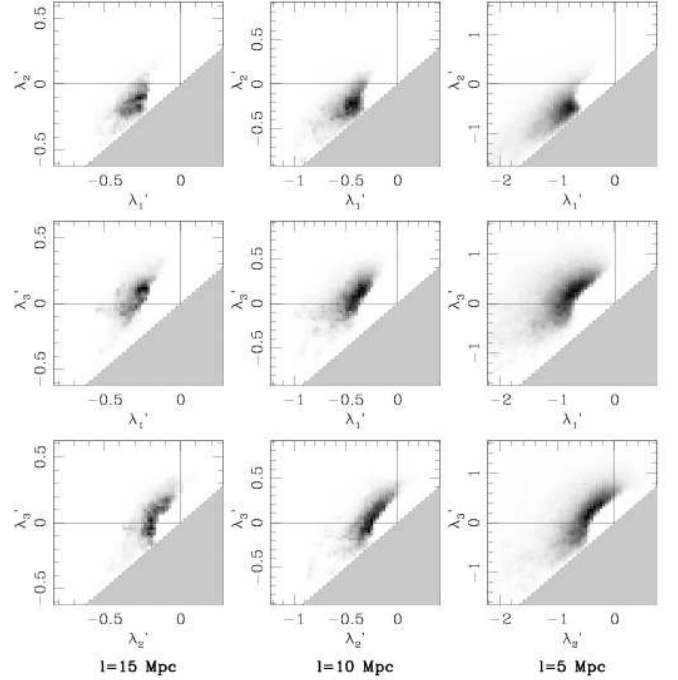


FIG. 6.— The same as Fig. 5, but for the $z = 1$ dark matter distribution.

In order to bring out these regions, Fig. 5 shows the λ -space distributions of dark matter after subtracting a gaussian random field with the same power spectrum (i.e. the difference between the columns in Fig. 4). Here, grayscale density maps replace contours and there is no colour-coding for real-space density, but only points with density greater than the mean are included. A comparison of these plots with the fingerprints in Fig. 1 will help us determine which structures dominate the dark matter distribution at each smoothing scale. Note that the axes of each plot have been scaled in proportion to the amplitude of the dimensionless power spectrum at the appropriate smoothing scale, allowing for a direct comparison of structural morphology between scales.

As shown in the righthand column of Fig. 1, the densest parts of clumps lie on the lower boundary of λ -space (dashed line) in all three projections. Filaments concentrate on the lower boundary of the $\lambda_2' - \lambda_1'$ projection, as do clumps, but filaments also concentrate along the x axis of the other two projections. In Fig. 5, we see that at both 15 and $10 h^{-1}$ Mpc scales, the points in Fig. 5 appear to be shifted up toward the x axis relative to the clump fingerprint. The distribution of points in the $\lambda_3' \text{ vs. } \lambda_1'$ projection is broad and extends to very negative values of λ_1' , consistent with the presence of filaments in addition to clumps. Overall, it appears that filaments are the dominant structure at $15 h^{-1}$ Mpc scales and $10 h^{-1}$ Mpc scales, with clumps beginning to dominate at $5 h^{-1}$ Mpc smoothing scales at $z = 0$.

There is no evidence for walls at $z = 0$ at the smoothing scales shown. Walls manifest themselves as an excess of points near both $\lambda_2' = 0$ and $\lambda_3' = 0$. Although they are difficult to distinguish from filaments in the $\lambda_3' \text{ vs. } \lambda_1'$ projection, there would be a clear overdensity of points along the x axis of the top plots of Fig. 4 and near the origin of the bottom plots if walls were dominant features.

The morphology of structures in the dark matter distribution changes significantly at higher redshifts, as shown in Figs. 6 ($z = 1$) and 7 ($z = 3$). In all three λ -space projections, the distribution is concentrated closer to the x axis at higher redshift, meaning that the larger eigenvalues decrease more rapidly than the smaller ones and overdensities are approaching spherical symmetry.

At $l = 15 h^{-1}$ Mpc, all of the plots are more sparsely populated

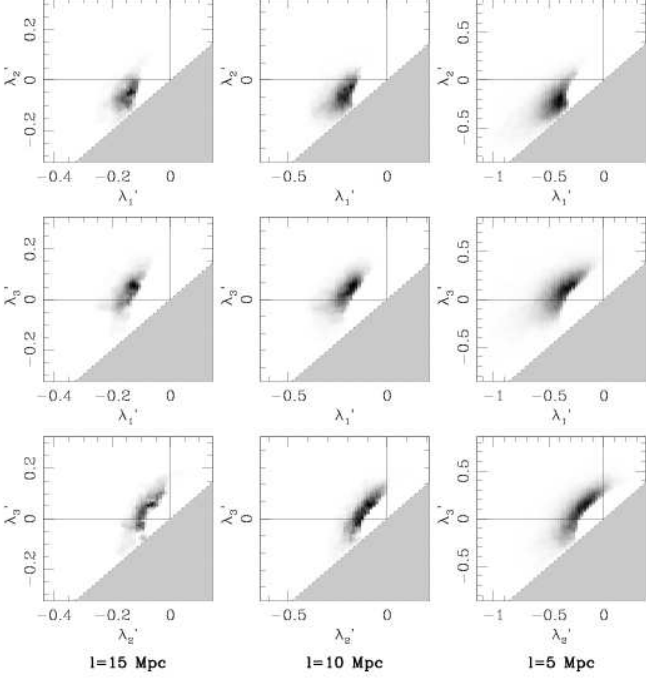


FIG. 7.— The same as Fig. 5, but for the $z = 3$ dark matter distribution. At $15 h^{-1}$ Mpc and $10 h^{-1}$ Mpc scales, distributions appear more wall-like than those at $z = 0$, suggested by a shift towards the $\lambda_2' = 0$ axis in the $\lambda_2' - \lambda_1'$ projection. Meanwhile, the λ -space distribution at $5 h^{-1}$ Mpc scales is more filamentary, as suggested by a similar shift toward the $\lambda_3' = 0$ axis in the bottom two projections. These latter projections are very similar to those for $15 h^{-1}$ Mpc scales at $z = 0$.

at high redshift, indicating that the λ -space distribution is closer to that of a gaussian random field. This is especially true of λ_3' vs. λ_2' , which also shows no dramatic change in shape out to $z = 1$. In the λ_3' vs. λ_1' , $l = 15 h^{-1}$ Mpc projection, the most densely populated regions retain their shape and relative contrast out to the highest redshifts, but some of the sparse features in the bottom left corner fade by $z \sim 1$. Finally, the upper left panel, λ_2' vs. λ_1' , undergoes dramatic evolution, with the tails at very negative eigenvalues disappearing and the bulk of the distribution moving to the $\lambda_2' = 0$ axis. In Fig. 1, we see that walls are most easily distinguishable from other structures in λ_2' vs. λ_1' , with points concentrated along $\lambda_2' = 0$. Taken together, these facts are suggestive of wall-to-filament evolution at a given comoving smoothing scale, with clumps developing by $z = 0$. The rapid fading of the λ_3' vs. λ_2' map is also explained, as walls are concentrated toward the origin in these two eigenvalues and would be indistinguishable from a gaussian random field. The signature of walls at high redshift are apparent in these plots, but they are of low contrast compared to the structures seen at smaller scales and lower redshift.

The two smaller smoothing lengths, $l = 10 h^{-1}$ Mpc and $l = 5 h^{-1}$ Mpc appear to be dominated by filament-to-clump evolution. In λ_3' vs. λ_2' , the distributions at both length scales exhibit a tail along the dashed boundary that grows toward $z = 0$. This tail is populated by the points near the dense centres of clumps. A similar tail exists in λ_3' vs. λ_1' , but here the growth of individual filamentary features is also evident, with a concentration near the $\lambda_3' = 0$ axis. It is interesting to compare the $z = 1$ projections for $l = 10 h^{-1}$ Mpc to the $z = 0$, $l = 15 h^{-1}$ Mpc projections. Their similarity suggests that the two length scales are in similar stages of non-linear evolution, but at different times. That the smaller length scales develop filamentary structure earlier is an indication of bottom-up structure formation; however, at a given comoving scale, structure evolves from walls to filaments to clumps, consistent with the ellipsoidal collapse picture

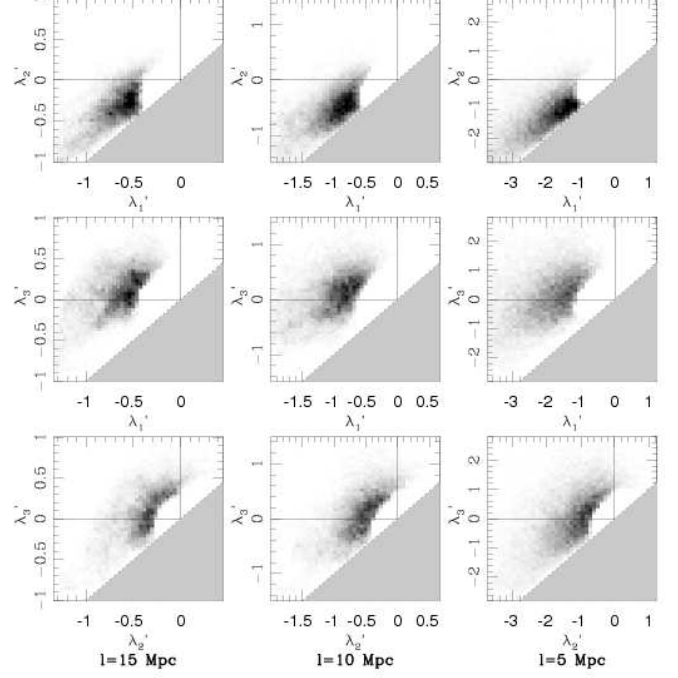


FIG. 8.— The λ -space projections for a $z = 0$ mock galaxy catalogue with $M_r < -20.5$, including redshift distortions.

of Zel'dovich (1970).

6.1. Mock catalogues in λ -space

In the SDSS data, we will be working with the observed galaxy distribution, so it is useful to generate λ -space projections for mock galaxies, generated by the methods described in § 4. There are many fewer galaxies than dark matter particles in the box volume, so the signal will be much weaker and shot noise may be non-negligible at $l = 5-10 h^{-1}$ Mpc scales. More importantly, there may be interesting differences between the large-scale structures appearing in the dark matter and galaxy distributions. In order to populate the dark matter haloes with galaxies, we must know the relevant halo occupation distribution (HOD, Berlind & Weinberg 2002); the probability, $P(N|M)$, that a halo of mass M will contain N galaxies.

Here we use the parametrization of Zheng, Coil, & Zehavi (2007), in which the probability of a halo of mass M containing a central galaxy is given by:

$$\langle N_{\text{cen}} \rangle = \frac{1}{2} \left[1 + \text{erf} \left(\frac{\log M - \log M_{\min}}{\sigma_{\log M}} \right) \right]. \quad (11)$$

Each central galaxy may be surrounded by one or more satellite galaxies, the mean number of which is given by,

$$\langle N_s \rangle = \frac{1}{2} \left[1 + \text{erf} \left(\frac{\log M - \log M_{\min}}{\sigma_{\log M}} \right) \right] \left(\frac{M - M_0}{M_1} \right)^\alpha. \quad (12)$$

The number of satellite galaxies in a given halo is drawn from a Poisson distribution and has no upper limit. The free parameters, M_{\min} , $\sigma_{\log M}$, M_0 , M_1 , and α have been derived from fits to SDSS galaxy catalogues. Table 1 of Zheng et al. 2007 provides the best-fitting HOD parameters for a series of absolute r -band magnitude cutoffs.

Once drawn from the relevant distributions, central galaxies are given the mean position and peculiar velocity of their associated dark matter halo, while satellite galaxies are each given the position and velocity of a randomly selected dark matter particle within the halo. When working with the SDSS data, we will construct a series of

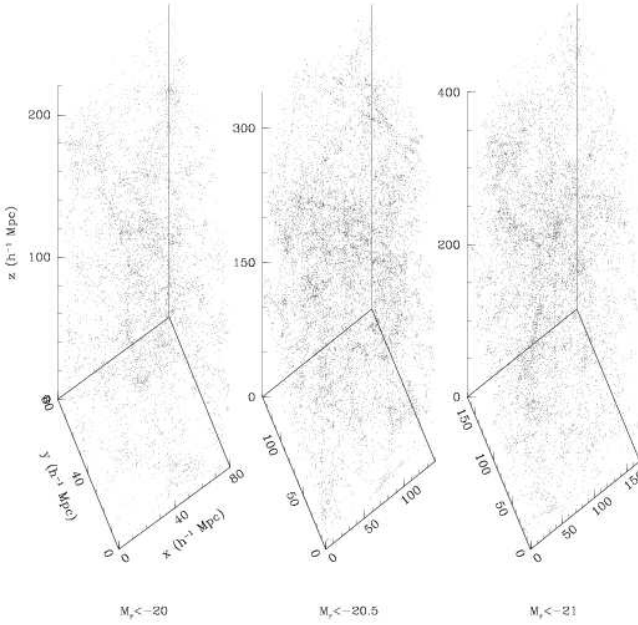


FIG. 9.— The three volume-limited samples taken from the SDSS VAGC large-scale structure sample, with galaxies placed at their comoving positions based on the concordance cosmology. The location of the Milky Way is $r = (250, -20, 110) h^{-1} \text{ Mpc}$, $r = (310, -20, 170) h^{-1} \text{ Mpc}$, and $r = (400, -25, 200) h^{-1} \text{ Mpc}$ in the Mr20, Mr205, and Mr21 samples, respectively, and the z axes are parallel to the Galactic North pole.

volume-limited samples, so the mock catalogues must be prepared to mimic the associated selection function.

One important difference between the redshift-space galaxy distribution and the dark matter distribution is the presence of fingers-of-god. These features, created by the peculiar velocities of galaxies in clusters, appear as very narrow filaments along the line of sight with widths $\sim 1 h^{-1} \text{ Mpc}$ and lengths up to $\sim 10 h^{-1} \text{ Mpc}$. The mock catalogues must contain a model of these redshift distortions if they are to properly mimic the SDSS data. The ‘distorted’ positions of galaxies are computed,

$$r_z = r + \frac{r \cdot v}{H_0} \hat{r}, \quad (13)$$

where r is the position in real space, v is the galaxy’s peculiar velocity, and \hat{r} is the unit radial vector between the observer and the galaxy.

In Fig. 8, we plot the λ -space projections of an $M_r < -20.5$ mock galaxy sample projected into redshift space. The redshift distortions are applied from a vantage point with coordinates $\{-300, 0, 100\} h^{-1} \text{ Mpc}$ relative to the origin of the box, selected to closely resemble the data samples constructed in the next section. The morphological characteristics of the λ -space distributions for $l = 15$ and $10 h^{-1} \text{ Mpc}$ are very similar to those of Fig. 5, though several features are different (for example, the smearing of the previously noted clump signature in the bottom left corner of λ'_3 vs. λ'_1). The changes are most noticeable at $l = 5 h^{-1} \text{ Mpc}$, particularly on the outskirts of the distributions. These regions are occupied primarily by clusters, which present fingers-of-god in redshift space, decreasing the magnitude of all three λ -values in their vicinity. The effect would of course be more dramatic with a smoothing length of $\sim 1 h^{-1} \text{ Mpc}$, comparable to cluster widths.

With the construction of the mock catalogues and the development of the theoretical framework presented in § 2, we now have all of the tools necessary to compare the real galaxy distribution to that predicted by the standard cosmological model. In the next section, we will present our galaxy sample, drawn from the SDSS, and use

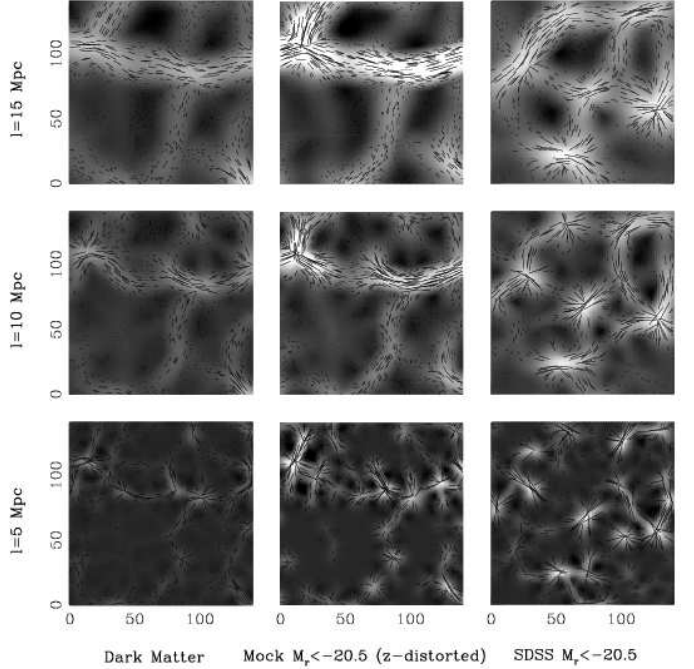


FIG. 10.— The two-dimensional λ'_1 distributions in slices from the $z = 0$ output of a ΛCDM cosmological simulation (dark matter and mock galaxy distributions, left and centre columns), and the SDSS galaxy distribution (right column), smoothed on a $15 h^{-1} \text{ Mpc}$ scale (top row), a $10 h^{-1} \text{ Mpc}$ scale (middle row) and a $5 h^{-1} \text{ Mpc}$ scale (bottom row). Bars have been plotted over the maps to indicate the direction of the axis of structure at each point in space. In all cases, the bar’s length is proportional to the magnitude of λ'_1 at that point. The grayscales are identical between the three columns. In all three samples and on all three smoothing scales, the axis of structure follows the minima in λ'_1 .

the λ -space distribution to make inferences about real large-scale structure.

7. FILAMENTS AND WALLS IN THE SDSS GALAXY DISTRIBUTION

The Sloan Digital Sky Survey has imaged a quarter of the sky in five wavebands, ranging from 3000 to 10000 \AA , to a depth of $r \sim 22.5$ (Abazajian et al. 2008). As of Data Release 7, spectra have been taken of $\sim 930,000$ galaxies, covering 8032 deg^2 and extending to Petrosian $r \sim 17.7$ (Strauss et al. 2002). Galaxy redshifts are typically accurate to $\sim 30 \text{ km s}^{-1}$, making it ideal for studies of large-scale structure. For this study, we need a portion of sky with relatively few coverage gaps to minimize the effect of the window function on the λ -space distributions. With this in mind, we construct three volume-limited subsamples from the northern portion ($8 < \alpha < 16 \text{ h}$ and $25 < \delta < 60$) of the NYU Value-Added Galaxy Catalogue (NYU-VAGC, Blanton et al. 2004, , through DR6), the first $80 \times 80 \times 220 (h^{-1} \text{ Mpc})^3$ in size with $M_r < -20$ (Mr20), another $140 \times 140 \times 340 (h^{-1} \text{ Mpc})^3$ in size with $M_r < -20.5$ (Mr205), and finally $170 \times 170 \times 400 (h^{-1} \text{ Mpc})^3$ in size with $M_r < -21$ (Mr21). Absolute magnitudes were computed with k_{correct} using SDSS Petrosian magnitudes shifted to $z = 0.1$ (and using $h = 1$). The sample properties of the galaxy distribution are given in Table 1 and the galaxy distributions are plotted in Fig. 9.

All boxes are padded with $30 h^{-1} \text{ Mpc}$ of empty space and binned on a $128 \times 128 \times 256$ grid, resulting in grid spacings of $1.09, 1.56$, and $1.80 h^{-1} \text{ Mpc}$ in the Mr20, Mr205, and Mr21 subsamples, respectively. To correct for edge effects, we define a window function on the same grid such that,

$$W_i = \begin{cases} 1 & \text{if } i \in S \\ 0 & \text{if } i \notin S \end{cases} \quad (14)$$

TABLE 1
SDSS SUBSAMPLES

Sample	Limiting M_r	Dimensions (h^{-1} Mpc)	N_g	Smoothing Scales (h^{-1} Mpc)
(1)	(2)	(3)	(4)	(5)
Mr20	-20	$80 \times 80 \times 220$	7105	5, 7, 10
Mr205	-20.5	$140 \times 140 \times 340$	14048	5, 10, 15
Mr21	-21	$170 \times 170 \times 400$	11499	15, 20, 25

where S is the set of grid points within the SDSS survey volume and i is a grid cell within the subsample volume. The above window function was computed by smoothing the sample boxes on a $20 h^{-1}$ Mpc scale and including in the window only those regions with densities more than 4 standard deviations below the mean density in the box. This is a crude approximation, but sample boxes were selected to lie in regions with few SDSS coverage gaps, so only a small fraction of grid cells are excluded (primarily near the box boundaries).

Once the window function and density fields have been computed on the grid, we smooth both with gaussian kernels on the scales given in Table 1, giving $\tilde{W}(x)$ and $\tilde{\rho}(x)$, respectively. The corrected density field is then

$$\rho'(x) = \frac{\tilde{\rho}(x)}{\tilde{W}(x)}. \quad (15)$$

The first and second derivatives of the density field have zero mean on large scales (if the cosmological principle holds) and the kernels used to compute them will integrate to zero. As such, there is no need to *renormalize* the smoothed derivative fields near the padded regions. Rather, we need only subtract the signal from the edge artificially introduced by the padding. That is,

$$H'_{ij} = \tilde{H}_{ij} - \tilde{\rho} \tilde{B}_{ij}, \quad (16)$$

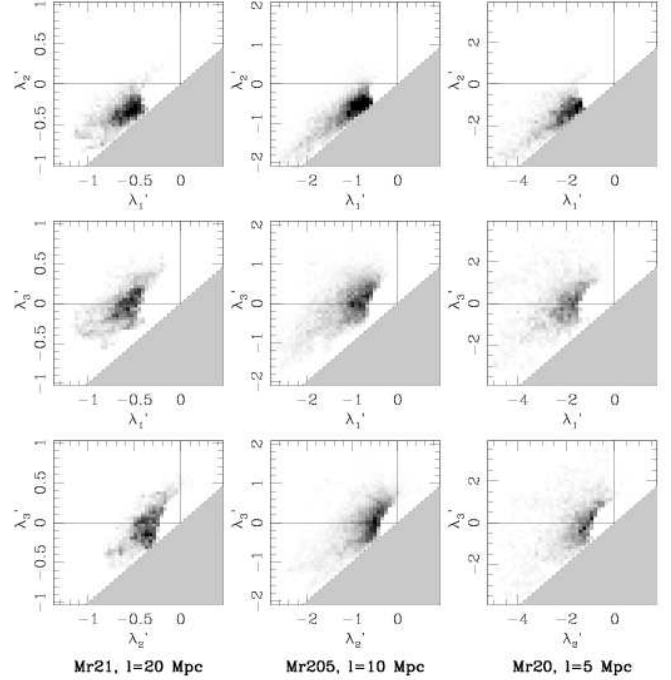
where \tilde{B}_{ij} is the matrix of smoothed second partial derivatives of the window function.

For each of the data samples listed in Table 1, we constructed a mock galaxy catalogue that matched the box dimensions, number density, padding, and redshift distortions of the SDSS data. The processing on the mock galaxy catalogues and the real data were identical and they should be directly comparable, with the caveat that the mock catalogues were taken from a $200 \times 200 \times 200$ (h^{-1} Mpc) 3 box periodic box, and therefore had to be repeated along the z axis in order to match the dimensions of the data subsamples. As such, finite-volume uncertainties will be larger in the simulations.

8. DISCUSSION

In Fig. 10, we compare the two-dimensional λ'_i maps between $10 h^{-1}$ Mpc thick slices from the $M_r < -20.5$ subsample, its corresponding mock catalogue, and the dark matter distribution. These data represent ~ 3 per cent of the $M_r < -20.5$ subsample and the normalization and range of the grayscales are identical between the two columns of each figure. The mean properties of each slice are superficially similar, although the slice from the mock catalogue has a large filament running through its centre, dominating the visual impression. In all maps, the axis of structure is oriented along edges in λ'_i , unlike the gaussian random field shown in Fig. 3.

The λ -space projections of the SDSS data are displayed in Fig. 11 for $l = 20 h^{-1}$ Mpc (Mr21), $l = 10 h^{-1}$ Mpc (Mr205), and $l = 5 h^{-1}$ Mpc (Mr21). For comparison, we present the corresponding λ -space distributions for the redshift space mock catalogues in Figs. 12. At small scales, the value of λ'_1/λ'_2 at the positions of galaxies is generally near unity (diagonal lines) and the distribution morphologies are similar to those in the mock catalogues. Shot noise is more severe at these scales than at larger scales, so the similarity



Mr21, $l=20$ Mpc Mr205, $l=10$ Mpc Mr20, $l=5$ Mpc

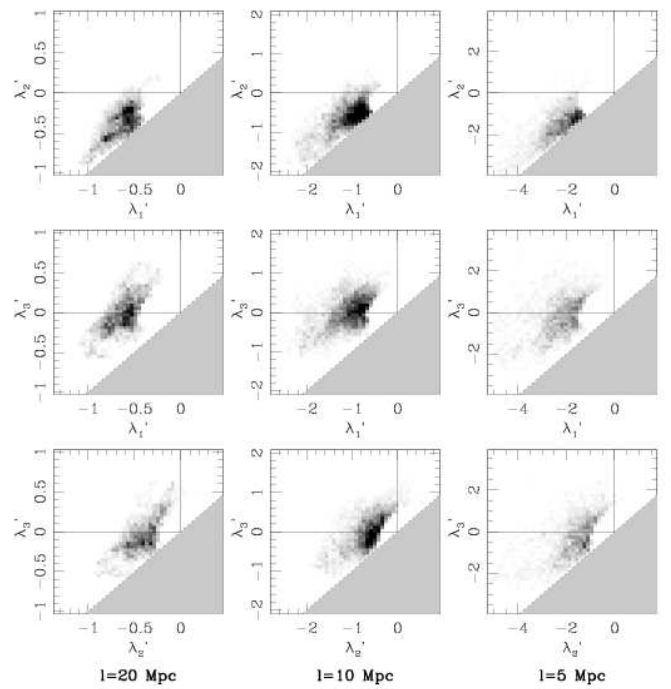


FIG. 12.— The same as Fig. 11, but for the mock galaxy samples. Grayscale and axis limits are the same between the two figures.

could be in part due to the extra power added by Poisson fluctuations. On $10 h^{-1}$ Mpc scales, there are some indications that the real galaxy distribution may be more evolved than the simulated one, as the distributions appear to have more outlying substructures, as well as a tail of clump-like objects with near-unity values of λ'_2/λ'_3 . If real, the discrepancy could suggest that the simulation is underestimating σ_8 .

Finite-volume effects are apparent at the larger smoothing scales for all of the samples. At the largest smoothing scales, there is clear evidence for non-linearity and the $\lambda'_2 - \lambda'_1$ projection shows evidence for both filaments and walls. Unlike the distributions at $l = 5 h^{-1}$ Mpc and $l = 10 h^{-1}$ Mpc, the data do not appear to be much more clump-like than the mock catalogues. However, there is some suggestion that the data are *less* wall-like on the largest scales (as suggested by the higher concentration of points on the $\lambda'_1 = \lambda'_2$ axis). This would also be consistent with a more evolved population, though finite-volume effects and uncertainties in the halo occupation distribution make it difficult to say for sure.

8.1. A matter of scale

Mention of large-scale structure often brings to mind images of narrow, interconnected filaments with clusters at the interstices weaving their way between vast cosmic voids. Bond et al. 1996 dubbed this mental image the ‘cosmic web’, but we have avoided using that phrase in this paper. The components of a spider web are strands, which come together at nodes to make a variety of complex structures on larger scales. The same could be said for filaments in the dark matter distribution, but that is not a complete picture. We also know that these filaments are made up of bound dark matter haloes. These small-scale filaments can themselves be the building blocks for large-scale ones.

Some recent attempts to quantify and identify individual filamentary structures have not taken the multiscale nature of structure into account. For example, minimal spanning tree algorithms (e.g., Barrow, Bhavsar, & Sonoda 1985; Colberg 2007) attempt to select filaments in the same manner as clusters, assuming that a step down up in linking length (that is, down in density contrast) will allow identification of the strands and full reconstruction of the web. Adaptive smoothing kernels and tessellation methods (e.g., Schaap & van de Weygaert 2000) enhance high-density regions in much the same way that simulations of galaxy formation adapt the mesh to treat star-forming regions, resulting in a nebulous combination of structure on small scales and large scales. There have also been attempts to use image segmentation (Aragón-Calvo et al. 2007) to select the most ‘prominent’ large-scale structures across a multitude of scales, and then remove them before looking for the next ones. Although this procedure makes sense *on a given scale*, removal of structures on one scale can cause one to miss structures on another.

We demonstrate the problem with this last approach using a $15 h^{-1}$ Mpc deep slice from the SDSS Mr20 subsample (Fig. 13). At smoothing scales of both $10 h^{-1}$ Mpc (upper right panel) and $3 h^{-1}$ Mpc (lower right panel), the axis of structure appears to be aligned with the λ'_1 ridges, suggesting that matter is condensed into filaments/walls on both scales (see Fig. 3). Furthermore, the filaments/walls found on the smaller scale appear to be components of those on larger scales. If the structures found on the $10 h^{-1}$ Mpc scale were removed before any of the smaller structures were identified, information would be lost. Conversely, if the smaller structures were all identified and removed first, there would be little left to find the larger ones.

In this paper, we have presented results on a number of smoothing scales and demonstrated how structure changed across those scales. Filaments appear to be present on scales ranging from at least $5 h^{-1}$ Mpc to $25 h^{-1}$ Mpc and are the dominant structures throughout most of that range. In Paper II, we extend these ideas by presenting a method to identify and characterize individual filaments.

8.2. Walls, walls, everywhere

There is evidence for a filament-to-clump progression as one smooths on progressively smaller scales in the $z = 0$ λ -space projections in both simulations and real data. Since smaller-scale overdensities collapse before larger ones, they should be in later stages of growth, so this progression may be a sign of ellipsoidal collapse. The collapse of a large-scale overdensity might still be expected to

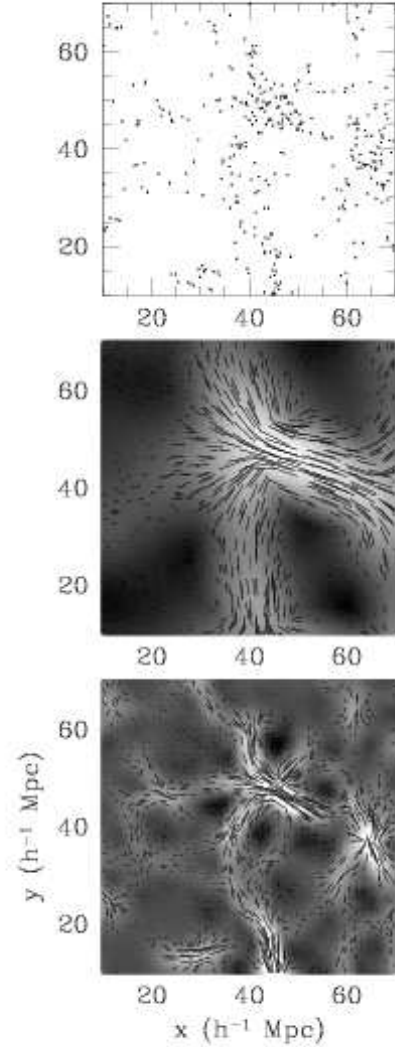


FIG. 13.— A two-dimensional demonstration of the structural hierarchy in a $15 h^{-1}$ Mpc deep slice from the SDSS Mr20 subsample. Galaxies are plotted in the upper left panel and λ'_1 grayscale maps are shown in the other two panels, smoothed on a $10 h^{-1}$ Mpc scale (upper right) and a $3 h^{-1}$ Mpc scale (lower right). Bars over the grayscale maps indicate the local direction of the axis of structure and their length is proportional to λ'_1 . Alignment of the axis of structure with the λ'_1 minima suggests that the structures are real on both scales (see Fig. 3). The filament- or wall-like structures seen on a $10 h^{-1}$ Mpc scale are divided into smaller filaments or walls on the $3 h^{-1}$ Mpc scale.

follow such a progression even if it were composed of smaller-scale condensed objects (such as dark matter haloes). The coherence of these large-scale filaments and walls would presumably depend upon the degree of fragmentation on intermediate scales.

One means of testing this picture is to look for walls in the very early stages of non-linear evolution. The $z = 0$ λ -space projections of the dark matter distribution show no convincing evidence for wall-like structures at scales as large as $15 h^{-1}$ Mpc, but they may still exist on larger scales or earlier times. The former is difficult to explore in our $200 h^{-1}$ Mpc simulation box, but we do have simulation outputs out to $z = 3$. In Fig. 14, λ'_1 maps for a $15 h^{-1}$ Mpc smoothing length are plotted for a range of redshifts, along with bars in

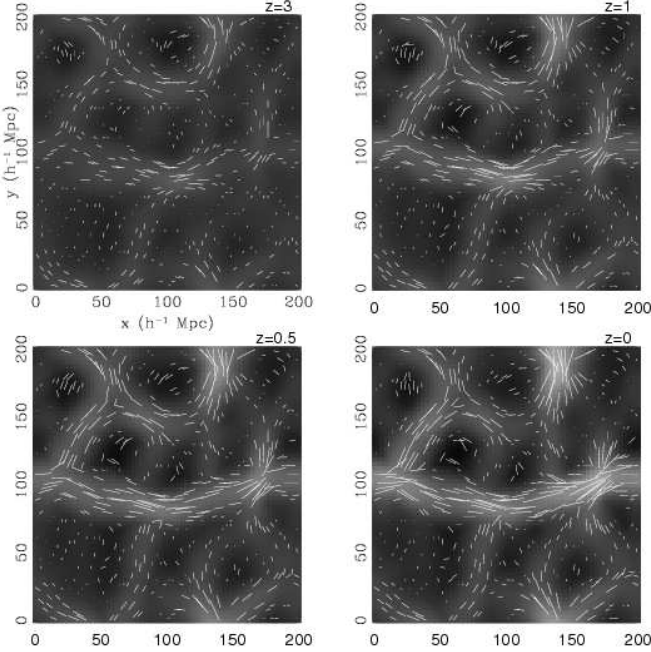


FIG. 14.— The λ'_1 grayscale maps for a series of $10 h^{-1}$ Mpc deep slices from the dark matter distribution, very similar to those in Fig. 3. The smoothing scale is $15 h^{-1}$ Mpc and maps are plotted for $z = 0, 0.5, 1$, and 3 . Bars indicate the direction of the axis of structure at random points on the grid, and the bar length is proportional to the local value of λ'_1 . In all maps shown here, the grayscale is scaled to the minimum and maximum of λ'_1 in the $z = 0$ map. The axis of structure aligns with minima in λ'_1 out to $z = 3$, unlike in gaussian random fields.

dicating the axis of structure. Even at $z = 3$, it is clear that, unlike in a gaussian random field, the axis of structure aligns with the λ'_1 edges (though it is impossible to distinguish filaments from walls in a two-dimensional projection). As discussed in § 6 and § 8.1, there appears to be a progression in both time and smoothing scale of wall-to-filament-to-clump. If this progression holds at $z = 0$, we might expect to see wall-like structures dominating on $\sim 40\text{--}50 h^{-1}$ Mpc scales.

The panels in the left-hand column of Fig. 15 show a subsample of dark matter particles in the $200 h^{-1}$ Mpc simulation box satisfying $\lambda'_1 < l_{\text{cut}}\sigma_{15}(z)$, where $\sigma_{15}^2(z)$ is the variance of the density field at a given redshift when smoothed on a $15 h^{-1}$ Mpc scale. Here, λ'_1 is measured with $15 h^{-1}$ Mpc smoothing and l_{cut} is a dimensionless constant. The cut isolates very similar regions of space at each redshift, but the distribution of matter within those structures evolves a great deal with time. The regions isolated by the cut are very sheet-like, and at $z = 3$ the matter is smoothly distributed within the structures. As the evolution progresses, they collapse into filamentary and clump-like structures.

Similarly, the right-hand column Fig. 15 shows particles in regions of small λ'_1 , but in a smaller box and on a smoothing scale of $5 h^{-1}$ Mpc. Here, structures have begun to collapse into filaments at $z = 3$ and by $z = 0$ are primarily concentrated in clumps. Despite the evolution of the structures within the regions selected by a cut in λ'_1 , the sizes and morphologies of the regions themselves change very little – they are still pancake-like at $z = 0$. This suggests that, even at low redshift, there should be evidence for wall-like structures in the galaxy and dark matter distributions on large scales, even if these walls are themselves made up of prominent filaments and clumps. As such, at all redshifts probed here, it can be the case that the majority of the mass in the universe is in walls on large scales, which are made up of filaments on smaller scales, which are made up of

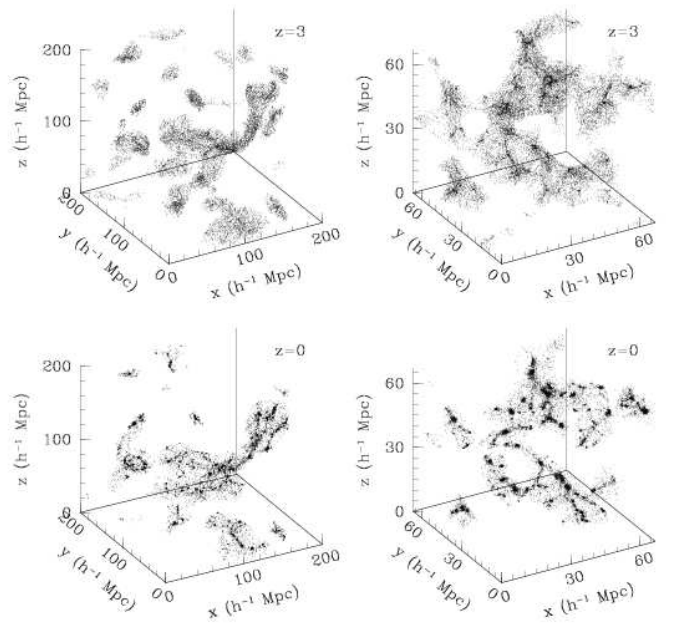


FIG. 15.— Selected dark matter particles in a $200 h^{-1}$ Mpc simulation box at $z = 0$ and $z = 3$. In the left column, particles are selected by the local value of $\lambda'_1/\sigma_{15}(z)$ after $15 h^{-1}$ Mpc gaussian smoothing. This cut follows individual structures as they evolve. Most of the structures are sheets/walls at $z = 3$, but have collapsed into filaments by $z = 0$. In the right column, $5 h^{-1}$ Mpc smoothing is used in a $67 h^{-1}$ Mpc box. On that scale, most of the structures are filamentary at $z = 3$, but have collapsed into clumps by $z = 0$.

clumps on still smaller scales.

8.3. Conclusions

With the eigenvalues and eigenvectors of the Hessian matrix, we can determine the type and orientation of structures in a continuous two- or three-dimensional density field. The ‘fingerprints’ of clumps, walls, and filaments in a three-dimensional space of eigenvalues (λ -space) provide templates for comparison to the large-scale matter distribution. In addition, as a result of non-linear growth of structure, the third Hessian eigenvector (which is used to define the ‘axis of structure’) aligns with the axis of filaments in both two and three dimensions, retaining this alignment within approximately one smoothing length from the central axis.

We drew three volume-limited subsamples from the northern portion of the SDSS spectroscopic survey (using the NYU-VAGC catalogue) and computed their Hessian parameter distributions on a range of length scales. These distributions were then directly compared to those found in a series of redshift-space mock galaxy catalogues generated from a cosmological simulation using the concordance cosmology. Results from this analysis include,

- The SDSS galaxy distribution is different from a gaussian random field on all smoothing scales used here (up to $25 h^{-1}$ Mpc), showing evidence for some combination of clusters, filaments, and walls on all of these scales.
- Filaments are the dominant structures on smoothing scales of $\sim 10 h^{-1}$ Mpc to $\sim 25 h^{-1}$ Mpc, though there is some evidence for a transition to wall-dominance at $\sim 25 h^{-1}$ Mpc. At $5 h^{-1}$ Mpc, clumps begin to dominate, but filaments are still apparent in the λ -space distributions.
- The axis of structure aligns with the minima in λ'_1 in projected slices, providing a signature of non-linear growth even when non-linearities are not apparent to the eye.

- The λ -space projections of the SDSS galaxy distribution are very similar to those expected in a Λ CDM universe with gaussian random phase initial conditions. There is some evidence that the data are clumpier than the simulations.
- In projected slices, the λ'_1 maps of the galaxy distribution are morphologically very similar to those of a gaussian random field. Since filaments and walls are oriented along minima in λ'_1 , this suggests that the outline for the filament network can be determined from the initial conditions.

To complement the results presented above for the SDSS galaxy distribution, we generated λ parameters at six redshifts in a Λ CDM cosmological N-body simulation, tracing the evolution of the matter distribution from $z = 3$ to $z = 0$. On comoving smoothing scales of $5 h^{-1}$ Mpc, filament-dominance at $z = 3$ gives way to clump-dominance at $z = 0$. At $z = 3$ and on comoving scales of $15 h^{-1}$ Mpc, the dark matter distribution is dominated by low-contrast walls, despite being only barely distinguishable from a gaussian random field in λ -space. Structure on this smoothing scale becomes filament-dominated by $z = 0$. Finally, in projected slices, the axis of structure follows the minima in λ'_1 on smoothing scales as large as $15 h^{-1}$ Mpc and epochs as early as $z = 3$. The same alignment is *not* seen in gaussian random fields.

The λ -space distributions of the galaxy density field are only a first step towards a more complete description of large-scale structure. In Paper II, we will describe a method for finding individual filamentary structures on a given scale, and then quantitatively evaluate the connection between filaments and galaxy clusters. Eventually, we hope to both extend our morphological studies to larger redshifts and to characterize the galaxy populations in structures on a range of scales. We will compare the SDSS λ -space distributions to those found in hydrodynamic simulations, test the dependence of the λ -space dis-

tributions on the cosmological model and galaxy HOD, look for a dependence of galaxy properties on the local geometry (Park et al. 2007), and compare the galaxy λ -space distribution to that of the hot gas (e.g. Phillips 2003).

9. ACKNOWLEDGMENTS

Funding for the SDSS and SDSS-II has been provided by the Alfred P. Sloan Foundation, the Participating Institutions, the National Science Foundation, the U.S. Department of Energy, the National Aeronautics and Space Administration, the Japanese Monbukagakusho, the Max Planck Society, and the Higher Education Funding Council for England. The SDSS Web Site is <http://www.sdss.org/>.

The SDSS is managed by the Astrophysical Research Consortium for the Participating Institutions. The Participating Institutions are the American Museum of Natural History, Astrophysical Institute Potsdam, University of Basel, University of Cambridge, Case Western Reserve University, University of Chicago, Drexel University, Fermilab, the Institute for Advanced Study, the Japan Participation Group, Johns Hopkins University, the Joint Institute for Nuclear Astrophysics, the Kavli Institute for Particle Astrophysics and Cosmology, the Korean Scientist Group, the Chinese Academy of Sciences (LAMOST), Los Alamos National Laboratory, the Max-Planck-Institute for Astronomy (MPIA), the Max-Planck-Institute for Astrophysics (MPA), New Mexico State University, Ohio State University, University of Pittsburgh, University of Portsmouth, Princeton University, the United States Naval Observatory, and the University of Washington.

We thank Jerry Ostriker for his many helpful comments and suggestions, Michael Blanton for his hard work and help with VAGC, and Jim Gunn, Neta Bahcall, and J. Richard Gott III for serving on the committee to the thesis of which this work was a part.

REFERENCES

Abazajian K., et al., 2008, preprint (astro-ph/0812.0649)
 Aragón-Calvo M. A., Jones B. J. T., van de Weygaert R., & van der Hulst J. M., 2007, A&A, 474, 315
 Barrow J. D., Bhavsar S. P., & Sonoda D. H., 1985, MNRAS, 216, 17
 Berlind A. A., & Weinberg D. H., 2002, ApJ, 575, 587
 Blanton M. R. et al., 2004, AJ, 129, 2562
 Bond J. R., Kofman L., & Pogosyan D., 1996, Nat, 380, 603
 Bond J. R., & Myers S. T., 1996, ApJS, 103, 1
 Bond N. A., 2008, PhD thesis, Princeton University
 Colberg J. M., 2007, MNRAS, 375, 337
 Colless M. et al., 2001, MNRAS, 328, 1039
 Davis M., Huchra J., Latham D. W., & Tonry J., 1982, ApJ, 253, 423
 Davis M., Efstathiou G., Frenk C. S., & White S. D., 1985, ApJ, 292, 371
 de Lapparent V., Geller M. J., & Huchra J. P., 1986, ApJS, 302, L1
 Dietrich J. P., Schneider P., Clowe D., Romano-Diaz E., & Kerp J., 2005, A&A, 440, 453
 Eisenstein D. J., & Hüt P., 1998, ApJ, 498, 137
 Frenk C. S., White S. D. M., & Davis M., 1983, ApJ, 271, 417
 Fry J. N., & Gaztanaga E., 1993, ApJ, 413, 447
 Huchra J. P., & Geller M. J., 1982, ApJ, 257, 423
 Gaztanaga E., & Frieman J. A., 1994, ApJ, 437, L13
 Geller M. J., & Huchra J. P., 1989, Sci, 246, 897
 Gott J. R., Jurić M., Schlegel D., Hoyle F., Vogeley M., Tegmark M., Bahcall N., & Brinkmann J., 2005, ApJ, 624, 463
 Guth A. H., 1981, Phys. Rev. D, 23, 347
 Guth A. H., & Pie S. Y., 1982, Phys. Rev. B, 115, 295
 Hahn O., Porciani C., Carollo M., & Dekel A., 2007, MNRAS, 375, 489
 Klypin A., & Shandarin S. F., 1993, ApJ, 314, 493
 Kulkarni G. V., Nichol R. C., Shet R. K., Seo H.-J., Eisenstein D. J., & Gray A., 2007, MNRAS, 378, 1196
 Martínez V. J., & Coles P., 1994, ApJ, 437, 550
 Massey R. et al., 2007, ApJS, 172, 239
 Nichol R. C. et al., 2007, MNRAS, 368, 1507
 Novikov D., Colombi S., & Doré O., 2006, MNRAS, 366, 1201
 Pan J., & Coles P., 2000, MNRAS, 318, L51
 Park C., Choi Y.-Y., Vogeley M. S., Gott J. R., & Blanton M. R., 2007, ApJ, 658, 898
 Peebles P. J. E., & Groth E. J., 1975, ApJ, 196, 1
 Phillips L. A., 2003, PhD thesis, Princeton University
 Press W. H., Flannery B. P., & Teukolsky S. A., 1986, Numerical Recipes. Cambridge Univ. Press, Cambridge
 Roberts S., Davies J., Sabatini S., Auld R., & Smith R., 2007, MNRAS, 379, 1053
 Ross A. J., Brunner R. J., & Myers A. D., 2007, ApJ, 665, 67
 Schaap W., & van de Weygaert R., 2007, A&A, 363, 29
 Shandarin S. F., & Yess C., 1998, ApJ, 505, 12
 Smith R. E. et al., 2003, MNRAS, 341, 1311
 Spergel D. N., et al., 2007, ApJS, 170, 377
 Starck J.-L., Martínez V. J., Donoho D. L., Levi O., Querre P., & Saar E., 2004, preprint (astro-ph/0406425)
 Stein M. L., 1997, in Feigelson E. D., Babu G. J., eds., Statistical Challenges in Modern Astronomy II. Springer-Verlag, New York, p. 166
 Strauss M. A., et al., 2002, AJ, 124, 1810
 Tanaka M., Hoshi T., Kodama T., & Kashikawa N., 2007, MNRAS, 379, 1546
 Thompson L. A., & Gregory S. A., 1978, ApJ, 220, 809
 Verde L., Heavens A. F., & Matarrese S., 2000, MNRAS, 318, 584
 York D. G., et al., 2000, ApJ, 120, 1579
 Zel'dovich Y. B., 1970, A&A, 5, 84
 Zel'dovich Y. B., Einasto J., & Shandarin S., 1982, Nat, 300, 407
 Zheng Z., Coil A. L., & Zehavi I., 2007, ApJ, 667, 760